Enhancing electrostatic interactions to activate polar molecules: ammonia borane methanolysis on a Cu/Co(OH)$_2$ nanohybrid†

Qian-Qian Chen, ‡[ac] Qiang Li, ‡[b] Chun-Chao Hou,[a] Chuan-Jun Wang,[a] Cheng-Yun Peng,[a] Núria López *[b] and Yong Chen *[ac]

Optimization of metal–support interactions (MSIs) is at the core of heterogeneous catalyst design. For polar reactants, electrostatic interactions resulting from MSIs can facilitate their activation. In this work, a feasible *in situ* method has been employed to control the electrostatic properties at the interface of a noble-metal-free Cu/Co(OH)$_2$ nanohybrid catalyst. On the Cu/Co(OH)$_2$ interface, the positively charged copper enhances the polar molecule adsorption. By varying the metal/support ratio, a highly efficient catalytic activity for the methanolysis of ammonia borane (AB) with an initial turnover frequency (TOF) of 61.63 $mol_{(H_2)}$ $mol_{(catalyst)}^{-1}$ min^{-1} and long-term stability at ambient temperature were observed. Theoretical analysis unravels the role of charge transfer in promoting the reactions and the metal/support ratio in manipulating the catalytic activity *via* tuning electrostatic interactions.

Introduction

For supported metal heterogeneous catalysts, their electronic and structural properties are modulated by metal–support interactions (MSIs) and determine their activity, selectivity and stability.[1–3] On metal-oxide supports, MSIs induce the dispersion of metal nanoparticles (NPs) to gain better stability against sintering and expose more active sites.[4–6] The synergetic effects promoting activity arise from the structural and charge transfer modifications occurring when the metal interacts with the support on the interface[7] and can be controlled by suitable choice of the synthetic protocol and pretreatments.[8–10] Furthermore, a rational design of candidates acting as carriers of metal NPs would simplify the preparation and promote the activity of catalysts *via* the dual functionalities of improving the dispersion[11,12] and regulating the electronic structure of metal NPs.[13,14]

Electronically, the charge transfer from the metal to the support results in electron depleted metal atoms which in return can facilitate the metal–reactant interactions. Molecules regarded as promising candidates for portable hydrogen chemical storage generally are non-polar without lone-electron pairs, (methane, ethane) and polar without empty π orbitals (methanol[15,16] and aminoborane, AB[17,18]). Since dipole–dipole interactions mainly contribute to the adsorption of these molecules on catalyst surfaces and the lack of stronger electronic interactions, the weak binding character limits their activation. However, for polar candidates, weak interactions based on electrostatic interactions are crucial to enhance their activation. For instance, high-performance catalysts in AB conversion are required to activate the B–N bond efficiently.[19,20] In our previous study, B–N bond breaking *via* an S_N2 mechanism was found to be the rate-limiting step in the reaction network, thus stronger AB adsorption with activated B–N bonds would promote this step.[21] As AB is a polar molecule, positively charged surface atoms would facilitate its adsorption and activation *via* electrostatic interactions, thus promoting its conversion.

Since the overall transferred charge is metal nanoparticle size dependent,[22] the electrostatic interactions with polar molecules can also be modulated by changing the amount of metal deposited. Experimentally, the metal nanoparticle size can be adapted *via* variable metal/support ratios, thus opening a path to control adsorption. Copper is an abundant coin metal and has been widely used in methanol synthesis.[23] Besides, Cu- and Co-based nanostructured materials[24,25] have been reported as good candidates for AB hydrolysis. However, the synergistic contributions of the Cu–support interface are still unclear thus limiting the controllability of the catalytic properties.

[a] *Key Laboratory of Photochemical Conversion and Optoelectronic Materials & HKU-CAS Joint Laboratory on New Materials, Technical Institute of Physics and Chemistry, Chinese Academy of Sciences, Beijing 100190, P. R. China. E-mail: chenyong@mail.ipc.ac.cn*

[b] *Institute of Chemical Research of Catolonia, ICIQ, The Barcelona Institute of Science and Technology, Ad. Països Catalans, 16, 43007, Tarragona, Spain. E-mail: nlopez@iciq.es*

[c] *University of Chinese Academy of Sciences, Beijing 100049, P. R. China*

† Electronic supplementary information (ESI) available. See DOI: 10.1039/c9cy00584f

‡ Qian-Qian Chen and Qiang Li contributed equally to this work.

In this work, a feasible *in situ* method which facilitates MSIs has been applied to synthesize a Cu/$Co(OH)_2$ nanohybrid catalyst. For the $Co(OH)_2$ support, its 2D layered structure endows it with the capacity to be an excellent support. Besides, the electron transfer or surface charges can be manipulated by varying the metal–support ratio. The optimized nanohybrid exhibits a high catalytic performance for AB methanolysis with an initial TOF of 61.63 $mol_{(H_2)}$ $mol_{(catalyst)}^{-1}$ min^{-1} and long-term durability at ambient temperature. Density functional theory (DFT) elucidates the promoting role of electrostatic interactions in the catalytic activity *via* stabilizing the AB adsorption and reducing the rate-determining step barrier for the OH^- attack *via* the S_N2 mechanism which initiates the reaction. Besides, the total catalytic activity which relies on the site activity and site numbers can be tuned *via* changing the metal/support ratio.

Experimental section

All chemicals and solvents were obtained commercially and used without further purification.

Synthesis of $Cu(OH)_2$

$Cu(OH)_2$ was synthesized by a simple precipitation method. Typically, 1 g $Cu(NO_3)_2{\cdot}6H_2O$ was dissolved in 20 mL deionized water with ultrasound to form a clear solution. Then the solution was slowly added dropwise into an 80 mL solution containing 2 g NaOH and 250 mg sodium citrate with intense magnetic stirring. After continuous magnetic stirring for 1 h, a colloidal dispersion was obtained. Finally, the sample was collected by centrifugation, then washed with water and ethanol, and dried in a vacuum at 60 °C for 6 h.

Synthesis of $Co(OH)_2$

The synthesis is the same as that of $Cu(OH)_2$ just by substituting $Cu(NO_3)_2{\cdot}6H_2O$ with $Co(NO_3)_2{\cdot}6H_2O$.

Synthesis of Cu/$Co(OH)_2$

Prior to the dehydrogenation experiment, $Cu(OH)_2$ and $Co(OH)_2$ with different mass ratios (the total mass weight of $Cu(OH)_2$ and $Co(OH)_2$ is 30 mg) were ground fully, recorded as $Cu(OH)_2/Co(OH)_2$. An AB solution with a certain concentration was injected into a 10 mL flask containing 10 mg $Cu(OH)_2/Co(OH)_2$ with a 5 mL syringe. Then the solution in the flask was vigorously stirred to obtain Cu/$Co(OH)_2$, which was used for further catalytic reaction. Catalysts with different mass ratios were synthesized with the same method, merely changing the mass ratio of $Cu(OH)_2$ to $Co(OH)_2$. Cu NPs were obtained with $Cu(OH)_2$ as a precursor under identical conditions.

Structural characterization

Powder X-ray diffraction (XRD) patterns were recorded on a Bruker AXS D8 X-ray diffractometer with Cu K_α (λ = 1.54056 Å, 100 mA and 40 kV). Raman spectroscopy measurements were performed on an inVia-Reflex confocal laser micro-Raman spectrometer using Ar^+ laser excitation (λ_{ex} = 532 nm). For X-ray photoelectron spectroscopy (XPS) analysis, the samples were first deoxygenated in Ar for at least 1 h and then investigated on a ThermoScientific ESCALAB 250XI spectroscope equipped with an Al K_α X-ray source and a power of 250 W was used. The charge effect was calibrated using the binding energy of C1s (284.8 eV). Transmission electron microscopy (TEM) and high resolution TEM (HRTEM) were conducted by using a JEM 2100F microscope with an accelerating voltage of 200 kV. For all TEM, HRTEM, and corresponding energy dispersive X-ray (EDX) analyses, the samples were first dispersed in ethanol and sonicated for at least 0.5 h, followed by dropping onto an ultrathin carbon film and leaving it to dry naturally at room temperature in air prior to these measurements. The Cu K-edge and Co K-edge absorption spectra were collected at the X-ray absorption fine structure (XAFS) station of the 1W1B beamline of the Beijing Synchrotron Radiation Facility.

Catalytic activity measurement

Dehydrogenation experiments in different solvents were performed in a 10 mL two-necked round-bottom flask, in which one neck was sealed with a rubber cap, while the other was connected to a gas burette. The temperature in the reaction system, which was confirmed by a thermometer, was maintained using a constant-temperature bath. A certain amount of catalyst was placed in the two-necked round-bottom flask, and 5 mL AB solution was quickly injected using a syringe. Before adding the catalyst, different amounts of $Cu(OH)_2$ and $Co(OH)_2$ were ground vigorously. The H_2 generated by the system was identified using a gas chromatograph (GC-14C, Shimadzu) equipped with a 5 Å molecular sieve column (3 m × 2 mm) and thermal conductivity detector; the carrier gas was Ar. The amount of gas was measured quantitatively, using a gas burette, to an accuracy of ±0.5 mL.

Computational details

A DFT study was employed by using the Vienna *ab initio* simulation package (VASP).[26,27] The exchange–correlation energies were obtained *via* the generalized gradient approximation with the Perdew–Burke–Ernzerhof functional (GGA-PBE).[28] The projector augmented wave (PAW)[29,30] with a cut-off energy of 450 eV was chosen to represent the inner electrons. A Γ-centered *k*-point mesh was generated through the Monkhorst–Pack method[31] with sampling denser than 0.03 $Å^{-1}$. Gas phase molecules were relaxed in a 20 × 20 × 20 $Å^3$ box. The optimized Cu bulk lattice parameter is 3.635 Å, in agreement with the experimental value of 3.615 Å.[32] A four layer $p(4 \times 4)$ slab model with a vacuum layer of 15 Å was used to simulate the (111) surface of the Cu catalyst. The topmost 2 layers were relaxed during the optimization while the remaining layers were kept fixed to mimic the bulk.

For the $Co(OH)_2$ support, due to the strongly correlated d orbitals of Co, additional on-site interactions were added to

correct the electron self-interaction by using the Coulomb interaction U and the electronic exchange J with Dudarev's approach of GGA+U,[33] which is implemented in the VASP code. The calculated bulk lattice parameters by using U_{eff} of 4.00 eV are 6.442 and 4.668 Å for a and c, respectively, in agreement with a and c values of 6.372 and 4.653 Å reported in the literature.[34] Besides, this value is close to the previously reported values in the range of U = 3.75–4.50 eV on Co^{2+} systems,[35–38] in spite of the fact that the predicted band-gap of 2.20 is lower than the recently reported experimental value of 2.87 eV (ref. 39) which depends on the material morphology.

Slab models of Cu(111), $Co(OH)_2$(0001), and four Co–Cu hetero-layer surfaces (see Fig. 1g) representing the pure copper, support and catalyst were applied to study the AB and methanol adsorption as well as transition states. The thresholds were 10^{-5} eV and 0.03 eV $Å^{-1}$ for electronic and ionic relaxations, respectively. The climbing image nudged elastic band method[40,41] (CI-NEB) was applied to locate the transition states in the rate determining steps. All the structures can be retrieved from ioChem-BD.[42,43]

Results and discussion

Morphological and structural analysis of $Cu/Co(OH)_2$

The unique $Cu/Co(OH)_2$ hybrid was firstly fabricated through a feasible *in situ* AB reduction strategy by taking the ground mixture of $Cu(OH)_2$ nanorods (NRs) (Fig. S3†) and $Co(OH)_2$ nanosheets (NS) (Fig. 1b) as precursors. As illustrated in Scheme 1, the $Cu(OH)_2$ NRs and $Co(OH)_2$ NSs were synthesized at room temperature by a simple wet-chemical method. The following $Cu/Co(OH)_2$, unless otherwise specified, refers to the sample synthesized with a mass ratio of $Cu(OH)_2$ and $Co(OH)_2$ of 7.0 : 3.0. After grinding them carefully, the as-prepared sample was directly used to catalyze the AB methanolysis. By taking advantage of the different intrinsic reduction potentials of the two metals ($E^0(Cu_{(II)/(I)})$ = +0.159 eV; $E^0(Cu_{(I)/(0)})$ = +0.520 eV; $E^0(Co_{(II)/(0)})$ = −0.280 eV all *vs.* SHE),[44,45] the $Cu(OH)_2$ NRs could be reduced to Cu NPs *in situ* by AB within several seconds, while $Co(OH)_2$ remains intact. This has been strongly evidenced by the XRD pattern with a diffraction peak at 43.3° assigned to the (111) plane of Cu NPs (Fig. 1a) and by the Raman spectra (Fig. S4†) with an

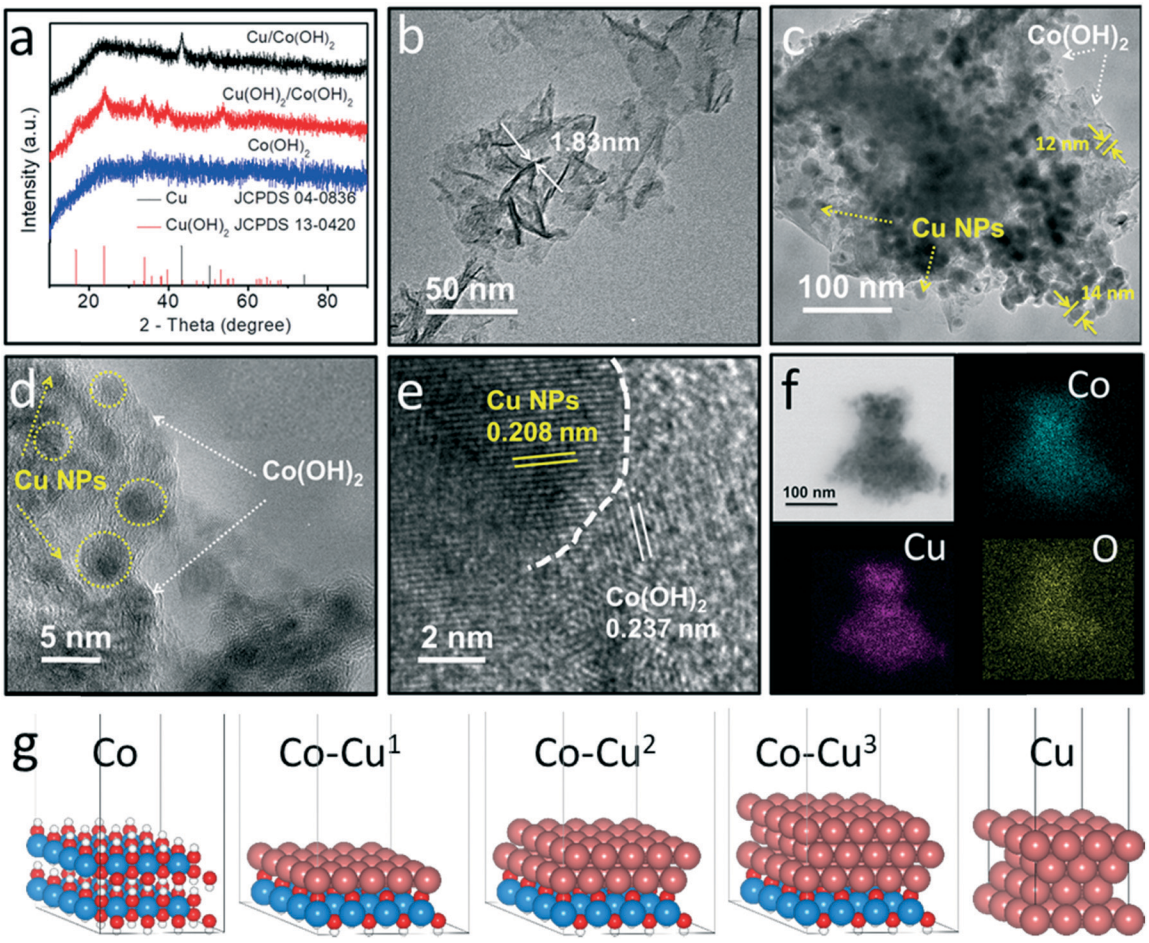

Fig. 1 (a) XRD patterns of the $Cu/Co(OH)_2$ hybrid, $Cu(OH)_2/Co(OH)_2$ and $Co(OH)_2$ NSs. (b) TEM image of $Co(OH)_2$. (c) TEM image of $Cu/Co(OH)_2$. (d) Magnified TEM and (e) HRTEM images of $Cu/Co(OH)_2$. (f) TEM elemental mapping images of Co, Cu and O for $Cu/Co(OH)_2$. (g) Slab models of the support and catalyst with different Cu/Co ratios Co–Cu^n where the superscript indicates the number of copper layers and pure Cu. Co, Cu, O, and H are shown in blue, brown, red, and white, respectively.

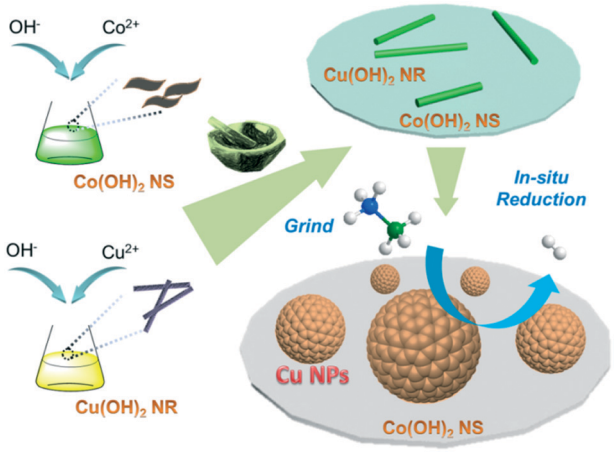

Scheme 1 Schematic illustration of the synthetic procedure of a Cu/$Co(OH)_2$ nanohybrid for AB methanolysis.

existing peak at 672 cm^{-1} corresponding to $Co(OH)_2$ (ref. 46) after the reduction process.

TEM images are obtained to further show the structural characteristics of $Cu/Co(OH)_2$. Fig. 1b shows the NS structure of $Co(OH)_2$ with a thickness of 1.83 nm. Compared with the bare Cu NPs with an average size of 33 nm (Fig. S5†), the Cu NPs in $Cu/Co(OH)_2$ show a smaller average size of 10 nm as shown in Fig. 1c and S6.† Fig. 1d further shows that Cu NPs are embedded on $Co(OH)_2$ with high dispersity. The smaller size and homogeneous dispersion of Cu NPs demonstrate that $Co(OH)_2$ can serve as a good anchoring site to disperse the NPs, which is more favourable to expose more active sites.[47] HRTEM was further carried out to better understand the interfacial structure of $Cu/Co(OH)_2$. In Fig. 1e, interplanar spacings of 0.208 nm and 0.237 nm are ascribed to Cu NPs and $Co(OH)_2$ NSs, respectively, indicating that $Co(OH)_2$ is retained and closely connected with Cu NPs. The corresponding elemental mapping of $Cu/Co(OH)_2$ further reveals the homogeneous distribution of Cu, Co, and O (Fig. 1f). All these characteristics prove that the *in situ* generated Cu NPs are well immobilized on the surface of $Co(OH)_2$ NSs. Theoretically, we built different representative slab models to interpret the experimental observations. These included a $Co(OH)_2$ structure either alone or with one Co replaced by Cu (Fig. S7†). Notice that the NPs are so large with an average size of 10 nm in Fig. 1c that the number of sites corresponding to steps or the perimeter is much smaller than that of planar sites (the ratio of the perimeter to surface is $1/R$, where R is the radius). Therefore, the reactivity can be directly explained from the planar centers without claiming the role of low-coordinated/defective sites. Water elimination from the $Co(OH)_2$ slab requires 2.89 eV and when one Co is replaced by a Cu atom, it is reduced to 2.24 eV, indicating that the $Co(OH)_2$ layers are robust under reaction conditions and will not generate oxygen vacancies. The results also imply that Cu sites would be easier to be reduced to NPs than Co sites. Alternatively, the Cu precursor can react with the $Co(OH)_2$ support to form covalent Co–O–Cu bonds by water elimination. Thus hetero-layer structures (Fig. 1g) with one to three Cu layers dispreading on CoO(OH) (labelled $Co–Cu^n$, n = 1–3) were used to study the Cu/Co ratio and interfacial effects on the catalytic behavior, with pure $Co(OH)_2(0001)$ and Cu(111) surfaces being the references. In these models, one Co layer was used as the support due to the fact that H bonds between the two interlayers have little effect on the electronic structures of the Co–Cu interface. The layered structures will explain the high dispersion and homogeneous distribution observed in Fig. 1f. The Cu–O and Cu–Cu bond energies are −0.44 and −0.29 eV, which were calculated from the standard formation enthalpy of Cu_2O (ref. 48) and Cu cohesive energy.[49] This suggests that the Cu dispersion on the $Co(OH)_2$ support is thermodynamically stable and also validates the hetero-layer models we have developed in this study. The calculated one Cu layer adsorption energies per atom on $Co–Cu^1$, $Co–Cu^2$ and Cu(111) surfaces are −0.98, −0.77 and −0.86 eV, respectively. This implies that when reducing $Cu(OH)_2$ the OH groups react with those of the $Co(OH)_2$ on the surface forming robust Cu–O–Co bonds. Once the first Cu layer on $Co(OH)_2$ is completed, Cu can further grow on it in a layer-by-layer fashion. The second layer is quite strongly bound to the Cu–O–Co bonds but the third layer is less attracted to them, probably because of the accumulated strain (12.852 Å of $p(5 \times 5)$-Cu(111) and 12.884 Å of $Co(OH)_2$) needed to match the $Co(OH)_2$ lattice. Therefore, both electronic and geometric effects limit the layer-by-layer epitaxial growth. When more Cu is present, NPs will form thus following a Stranski–Krastanov growth.[50]

Electronic structure of the catalysts

X-ray absorption near edge structure (XANES) spectroscopy, extended X-ray absorption fine structure (EXAFS) spectroscopy and XPS are performed to further understand the valence state and electronic structure of $Cu/Co(OH)_2$. In Fig. 2a, a similar pre-edge feature and shape for $Cu/Co(OH)_2$ and Cu foil confirm the formation of Cu NPs.[51] The Cu–O bonds in Fig. 2b can be from the interface between Cu NPs and the $Co(OH)_2$ surface. In addition, the inevitably oxidized Cu on the surface would also contribute to the Cu–O peak because of its easily oxidizable nature and unavoidable exposure to air during sample preparation. As shown in Fig. S8,† peaks at 934.4 eV and 954.4 eV assigned to Cu(II) can be observed in the spectra of $Cu(OH)_2$ and $Cu(OH)_2/Co(OH)_2$, and peaks at lower binding energies appear in the spectrum of $Cu/Co(OH)_2$, demonstrating the existence of reduced Cu in the $Cu/Co(OH)_2$ hybrid. Further, Cu 2p high-resolution XPS of $Cu/Co(OH)_2$ gives a strong proof that Cu(II) is reduced to Cu(0) (Fig. 2c). In detail, the major peaks at 932.4 and 952.4 eV are well assigned to the $2p_{3/2}$ and $2p_{1/2}$ of Cu(0).[52,53] And the other peaks at 934.4 and 954.4 eV along with two satellite peaks are the characteristic signals of CuO,[54] due to the surface oxidation. The pre-edge of $Cu/Co(OH)_2$ at 7709 eV (ref. 55) (Fig. S9†) and the peak at 780.6 eV (ref. 56) (Fig. S10†) all prove that Co remains +2.

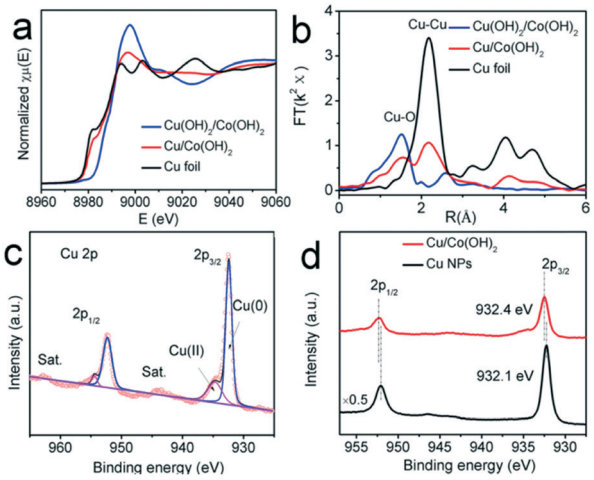

Fig. 2 (a) Cu *k*-edge XANES and (b) Fourier transforms of k^2-weighted Cu EXAFS spectra of $Cu(OH)_2/Co(OH)_2$, $Cu/Co(OH)_2$ and Cu foil. (c) High-resolution XPS spectrum of Cu in $Cu/Co(OH)_2$. (d) Cu 2p XPS spectra of $Cu/Co(OH)_2$ and Cu NPs.

XPS provides more powerful evidence of changes in the electronic structure arising from the MSI between Cu NPs and $Co(OH)_2$. As shown in Fig. 2d, the binding energy of Cu in $Cu/Co(OH)_2$ is positively shifted to about 0.3 eV compared with bare Cu NPs. Also, the Cu absorption edge of the magnified XANES spectra in Fig. S11 (ESI†) shows a positive shift in $Cu/Co(OH)_2$ compared with that in $Cu(OH)_2/Co(OH)_2$. The higher binding energy and positive shift of the Cu absorption edge indicate the change in the electronic structure of Cu NPs in $Cu/Co(OH)_2$ which are then electron deficient. Moreover, the core-level shift[57] of Cu from Cu(111) to Co–Cu^3 is 0.26 eV (see eqn (S2)†), demonstrating the charge transfer on the interface and the reliability of our theoretical model in describing the electronic properties in this system. For the Co 2p XPS spectra (Fig. S10†), the binding energy of Co in $Cu/Co(OH)_2$ shows a small negative shift, compared with that in $Cu(OH)_2/Co(OH)_2$. Based on these results, we conclude that the MSI exists when Cu NPs are coupled with the $Co(OH)_2$ support resulting in the decrease of the electron density of Cu NPs in $Cu/Co(OH)_2$.

Activity evaluation of $Cu/Co(OH)_2$ and theoretical analysis

The methanolysis of AB under alkaline conditions was applied to evaluate the activity of the as-prepared $Cu/Co(OH)_2$. AB is a promising candidate for hydrogen storage due to its integrated advantages of high hydrogen content (19.6 wt%, 146 g L^{-1}), long-term stability and non-toxicity.[24,58] About three equivalents of hydrogen are released per equivalent of AB. Meanwhile, the broad resonance assigned to ammonium tetramethoxyborate at 8.79 ppm (ref. 59) (Fig. S13†) demonstrates that the methanolysis occurred according to the following equation.

$$NH_3BH_3 + 4MeOH \rightarrow NH_4B(OMe)_4 + 3H_2 \quad (1)$$

The ratio of Cu in the hybrid catalyst was tuned by varying the initial mass ratios of $Cu(OH)_2$ to $Co(OH)_2$ ranging from 3.0 : 7.0 to 9.0 : 1.0 (Fig. 3a). The optimized ratio of 7.0 : 3.0 achieves the highest catalytic activity. As shown in Fig. 3b and c, the $Cu/Co(OH)_2$ hybrid has a drastically improved activity compared with their bare counterparts, demonstrating that the MSI in $Cu/Co(OH)_2$ can bring a positive synergy for AB methanolysis. $Co(OH)_2$ is almost inactive, which is also confirmed by our theoretical studies. DFT calculated adsorption energies of AB (−0.42 eV) and methanol (−0.10 eV) on $Co(OH)_2$ are in the range of physisorption, implying that the reactants are rather weakly bonded to the surface and not activated. The experimental and theoretical results prove that Cu is the real activity site for AB methanolysis.

To explore the reaction kinetics, a series of experiments with various molar ratios of catalyst/AB were performed carefully. Compared with the concentration of AB with half-order kinetics, the hydrogen production rate is more dependent on the concentration of $Cu/Co(OH)_2$, following the first-order kinetics. The maximum initial TOF of 61.63 $mol_{(H_2)}$ $mol_{(catalyst)}^{-1}$ min^{-1} (88.04 $mol_{(H_2)}$ $mol_{(Cu)}^{-1}$ min^{-1}) was obtained at a catalyst/AB molar ratio of 0.129 at room temperature (Fig. S14†). In addition, the apparent activation energy (E_a) obtained from the temperature dependent methanolysis reaction is 37.6 kJ mol^{-1} based on the Arrhenius equation (Fig. S15†).

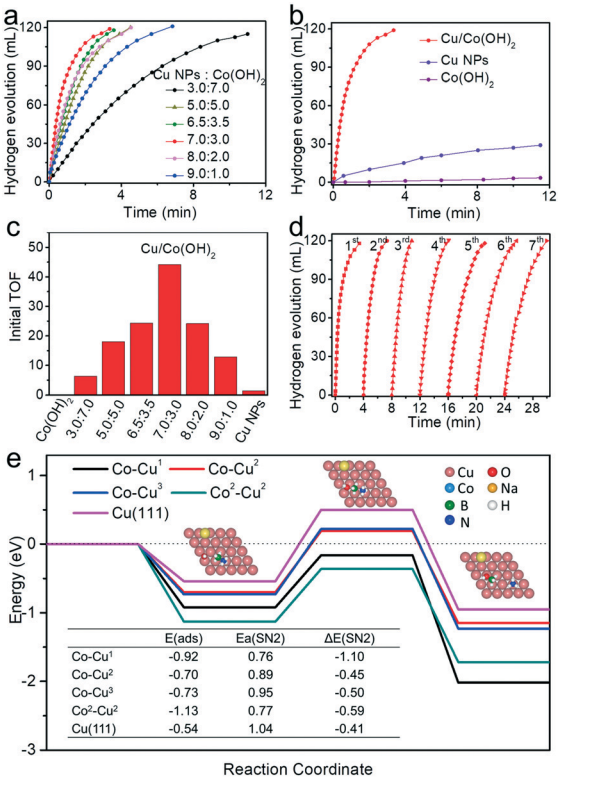

Fig. 3 (a) Stoichiometric hydrogen evolution in 0.5 M NaOH methanol solution catalyzed by as-prepared $Cu/Co(OH)_2$ with different mass ratios of the $Cu(OH)_2$ and $Co(OH)_2$ precursors. (b) Hydrogen evolution for $Cu/Co(OH)_2$, Cu NPs and $Co(OH)_2$. (c) Corresponding TOFs based on the total mol of metal. (d) Recycling of the $Cu/Co(OH)_2$ catalyst (8 mg) in 0.5 M NaOH methanol solution (5 mL), with addition of AB (1.62 mmol) to the system at 298 K in each cycle. (e) Adsorption of AB and the reaction coordinate for the S_N2 steps on Cu(111) and Co–Cu heterostructures.

Moreover, the Cu/$Co(OH)_2$ hybrid shows a comparable stability as shown in Fig. 3d.

From a theoretical point of view, the stronger adsorption energy of reactants and lower reaction barriers on the $Co(OH)_2$ supported Cu NPs explain the excellent methanolysis of AB caused by the synergy between Cu NPs and $Co(OH)_2$ NSs. For the adsorption on Cu(111), methanol is weakly bonded with an energy of −0.22 eV, in agreement with a previous estimate of −0.19 eV (ref. 60) while that of AB is −0.54 eV. On the Co–Cu^{1-3} model, AB and methanol coordinations are enhanced by 0.20–0.30 eV (Table S3†). The origin of the stronger bond can be traced back to electrostatic interactions as both AB and methanol are polar molecules and in the Co–Cu^{1-3} heterostructures the Cu layers are positively charged according to the Bader charges (per atom) of 0.28, 0.14, and 0.10 $|e^-|$, thus the Cu(111) surface is electron deficient and exhibits the δ^+ character which promotes the dipole–dipole interaction between the surface and molecules. Recently, electrostatic interaction-enhanced C_1 oxygenate adsorption energies on an Au/MgO substrate have been reported by Greeley *et al.*[61] In the AB conversion, our previous study shows that the S_N2 step (hydroxyl attack) is the rate determining step.[21] The transition states of the S_N2 on these four surfaces (Cu(111), Co–Cu^{1-3} models) show that barriers decrease from 1.04, to 0.95 to 0.89 and to 0.76 eV, respectively, when reducing the number of Cu layers (Fig. 3e).

For the initial and transition states of BH_3NH_3 species on these four surfaces, the average Bader charges of N atoms are negative and decrease from 1.37 to 1.17 $|e^-|$ (Table S4†), showing the electron transfer from N to the surface when the B–N bond breaks. The results above imply that the reactants are activated and the barrier for rate limiting steps is lowered on Cu/$Co(OH)_2$. As shown in Fig. 3e, the lower the number of layers, the better the desorption towards the S_N2 reaction balance and the more active the system. According to the experiments a volcano activity plot is observed in Fig. 3c. Our DFT results above can explain this dependence. The $Co(OH)_2$ layers are stacked by only 0.073 eV per Co atom, which means that the Co layers can open and react with the Cu precursor to form the Cu layers on the support. If the layers are self-limited in the growth then the maximum wetting between the Cu and the Co will be achieved for an atomic ratio of around 3 (50 : 16) that would represent the maximum number of the most active Cu sites. Therefore, a sandwich model with two layers of Cu on two sides of $Co(OH)_2$ (Co^2–Cu^2) has been optimized. The AB adsorption on Co^2–Cu^2 is further strengthened by 0.21 eV and the barrier for the S_N2 step is slightly increased by 0.01 eV. From these values, the apparent activation energy would be between 24.8–44.1 kJ mol^{-1} once the AB solvation has been taken into account. When the mass ratio increases, the activity decreases which can be inferred from the reactions on Co–Cu^2 and Co–Cu^3 surfaces with more Cu layers. For ratios smaller than 7.0 : 3.0, the number of active sites limits the activity. Thus, the number of active sites and the relative reactivity of the different sites, work together in determining the catalytic behaviour. Since they have opposite trends upon varying the mass ratio, the highest TOF value is reached when the maximum number of sites with the highest reactivity is achieved.

Conclusions

In summary, by changing the metal/support ratio in a Cu/$Co(OH)_2$ nanohybrid, a simple and rational strategy to control the reactant–surface electrostatic interactions *via* MSIs has been applied. On the one hand, the activity enhancement arises from the more exposed active sites of Cu NPs immobilized on the $Co(OH)_2$ NS support and positively charged Cu atoms which strengthen the electrostatic interactions with AB. On the other hand, the site activity is reduced upon increasing the Cu content in the synthetic steps due to the fact that the denser Cu layers have less positively charged atoms. By varying the Cu/Co ratio, the catalytic performance is controllable and at a ratio of 7.0 : 3.0, the Cu/$Co(OH)_2$ catalyst shows an excellent catalytic performance towards methanolysis of AB with an initial TOF of 61.63 $mol_{(H_2)}$ $mol_{(catalyst)}^{-1}$ min^{-1} under alkaline conditions. And this has been further confirmed by our DFT calculations *via* the hetero-layer models; electron transfer from Cu to the support *via* the Cu–O bonds results in positively charged Cu, increasing the electrostatic interaction between Cu and adsorbates, and also reduces the barriers of the rate-limiting step, the S_N2 hydroxyl attack. Since molecules in portable hydrogen storage applications are generally polar, saturated and do not have strong electronic interactions with the catalyst, this protocol would be applied for polar energy vector activation.

Conflicts of interest

There are no conflicts to declare.

Acknowledgements

The financial support from the Strategic Priority Research Program of the Chinese Academy of Sciences (XDB17000000), the Natural Science Foundation of China (21773275) and the CAS-Croucher Funding Scheme for Joint Laboratories is deeply acknowledged. We also acknowledge the help from the 1W1B beamline of Beijing Synchrotron Radiation Facility in XANES and EXAFS characterization. Q. L. and N. L. are grateful to the project CTQ2015-68770-R from the Spanish Ministerio de Economía y Competitividad (MINECO) for financial support and the Barcelona Supercomputing Centre (BSC-RES) for providing generous computer resources. The authors appreciate the kind discussions with Mr. G. Tang from Beijing Institute of Technology and Prof. X. Ming from Guilin University of Technology.

Notes and references

1 H. L. Tang, Y. Su, B. S. Zhang, A. F. Lee, M. A. Isaacs, K. Wilson, L. Li, Y. G. Ren, J. H. Huang, M. Haruta, B. T. Qiao, X. Liu, C. Z. Jin, D. S. Su, J. H. Wang and T. Zhang, *Sci. Adv.*, 2017, 3, e1700231.

2 S. J. Tauster, *Acc. Chem. Res.*, 1987, **20**, 389–394.
3 L. Liu and A. Corma, *Chem. Rev.*, 2018, **118**, 4981–5079.
4 J. A. Farmer and C. T. Campbell, *Science*, 2010, **329**, 933–936.
5 M. Cargnello, V. V. T. Doan-Nguyen, T. R. Gordon, R. E. Diaz, E. A. Stach, R. J. Gorte, P. Fornasiero and C. B. Murray, *Science*, 2013, **341**, 771–773.
6 T. C. Campbell, *Nat. Chem.*, 2012, **4**, 597–598.
7 N. Russo and D. R. Salahub, *Springer Science & Business Media*, 2012, vol. 546, pp. 49–71.
8 M. Flytzani-Stephanopoulos and B. C. Gates, *Annu. Rev. Chem. Biomol. Eng.*, 2012, **3**, 545–574.
9 R. Subbaraman, D. Tripkovic, D. Strmcnik, K. C. Chang, M. Uchimura, A. P. Paulikas, V. Stamenkovic and N. M. Markovic, *Science*, 2011, **334**, 1256–1260.
10 J. C. Matsubu, S. Y. Zhang, L. DeRita, N. S. Marinkovic, J. G. Chen, G. W. Graham, X. Q. Pan and P. Christopher, *Nat. Chem.*, 2017, **9**, 120–127.
11 X. Ma, Y. X. Zhou, H. Liu, Y. Li and H. L. Jiang, *Chem. Commun.*, 2016, **52**, 7719–7722.
12 Y. H. Zhou, Q. Yang, Y. Z. Chen and H. L. Jiang, *Chem. Commun.*, 2017, **53**, 12361–12364.
13 L. Dai, Q. Qin, P. Wang, X. J. Zhao, C. Y. Hu, P. X. Liu, R. X. Qin, M. Chen, D. H. Ou, C. F. Xu, S. G. Mo, B. H. Wu, G. Fu, P. Zhang and N. F. Zheng, *Sci. Adv.*, 2017, **3**, e1701069.
14 J. X. Feng, L. X. Ding, S. H. Ye, X. J. He, H. Xu, Y. X. Tong and G. R. Li, *Adv. Mater.*, 2015, **27**, 7051–7057.
15 G. A. Olah, *Angew. Chem., Int. Ed.*, 2013, **52**, 104–107.
16 L. Lin, W. Zhou, R. Gao, S. Yao, X. Zhang, W. Xu, S. Zheng, Z. Jiang, Q. Yu, Y. W. Li, C. Shi, X. D. Wen and D. Ma, *Nature*, 2017, **544**, 80–83.
17 Q. Xu and M. Chandra, *J. Power Sources*, 2006, **163**, 364–370.
18 C. Y. Peng, C. C. Hou, Q. Q. Chen, C. J. Wang, X. J. Lv, J. Zhong, W. F. Fu, C. M. Che and Y. Chen, *Sci. Bull.*, 2018, **63**, 1583–1590.
19 Q. Sun, N. Wang, R. Bai, Y. Hui, T. Zhang, D. A. Do, P. Zhang, L. Song, S. Miao and J. Yu, *Adv. Sci.*, 2019, 1802350.
20 C. Y. Peng, L. Kang, S. Cao, Y. Chen, Z. S. Lin and W. F. Fu, *Angew. Chem., Int. Ed.*, 2015, **54**, 15725–15729.
21 C. C. Hou, Q. Li, C. J. Wang, C. Y. Peng, Q. Q. Chen, H. F. Ye, W. F. Fu, C. M. Che, N. López and Y. Chen, *Energy Environ. Sci.*, 2017, **10**, 1770–1776.
22 T. Ioannides and X. E. Verykios, *J. Catal.*, 1996, **161**, 560–569.
23 J. T. Gallagher and J. M. Kidd, *UK1159035*, 1966.
24 W. W. Zhan, Q. L. Zhu and Q. Xu, *ACS Catal.*, 2016, **6**, 6892–6905.
25 K. Feng, J. Zhong, B. Zhao, H. Zhang, L. Xu, X. Sun and S. T. Lee, *Angew. Chem., Int. Ed.*, 2016, **55**, 11950–11954.
26 G. Kresse and J. Furthmüller, *Comput. Mater. Sci.*, 1996, **6**, 15–50.
27 G. Kresse and J. Furthmüller, *Phys. Rev. B: Condens. Matter Mater. Phys.*, 1996, **54**, 11169–11186.
28 J. P. Perdew, K. Burke and M. Ernzerhof, *Phys. Rev. Lett.*, 1996, **77**, 3865–3868.
29 P. E. Blöchl, *Phys. Rev. B: Condens. Matter Mater. Phys.*, 1994, **50**, 17953–17979.
30 G. Kresse and D. Joubert, *Phys. Rev. B: Condens. Matter Mater. Phys.*, 1999, **59**, 1758–1775.
31 H. J. Monkhorst and J. D. Pack, *Phys. Rev. B: Solid State*, 1976, **13**, 5188–5192.
32 D. Lide, *CRC Handbook of Chemistry and Physics*, CRC Press, Boca Raton, FL, 84th edn, 2003–2004, pp. 19–21.
33 S. L. Dudarev, G. A. Botton, S. Y. Savrasov, C. J. Humphreys and A. P. Sutton, *Phys. Rev. B: Condens. Matter Mater. Phys.*, 1998, **57**, 1505.
34 F. Pertlik, *Monatsh. Chem.*, 1999, **130**, 1083–1088.
35 M. Capdevila-Cortada, Z. Łodziana and N. López, *ACS Catal.*, 2016, **6**, 8370–8379.
36 J. Chen, X. Wu and A. Selloni, *Phys. Rev. B: Condens. Matter Mater. Phys.*, 2011, **83**, 245204.
37 A. L. Dalverny, J. S. Filhol, F. Lemoigno and M. L. Doublet, *J. Phys. Chem. C*, 2010, **114**, 21750–21756.
38 M. Aykol and C. Wolverton, *Phys. Rev. B: Condens. Matter Mater. Phys.*, 2014, **90**, 115105.
39 K. Kongsawatvoragul, S. Kalasina, M. Suksomboon, N. Phattharasupakun, J. Wutthiprom, T. Sudyoadsuk, V. Promarak and M. Sawangphruk, *ECS Trans.*, 2018, **85**, 1203–1217.
40 G. Henkelman and H. Jónsson, *J. Chem. Phys.*, 2000, **113**, 9978–9985.
41 G. Henkelman, B. P. Uberuaga and H. Jónsson, *J. Chem. Phys.*, 2000, **113**, 9901–9904.
42 M. Álvarez-Moreno, C. de Graaf, N. López, F. Maseras, J. M. Poblet and C. Bo, *J. Chem. Inf. Model.*, 2014, **55**, 95–103.
43 Q. Li and N. López, Enhancing Electrostatic Interactions to Activate Polar Molecules: Ammonia Borane Methanolysis on $Cu/Co(OH)_2$ Nanohybrid, DOI: 10.19061/iochem-bd-1-93.
44 J. M. Yan, X. B. Zhang, T. Akita, M. Haruta and Q. Xu, *J. Am. Chem. Soc.*, 2010, **132**, 5326–5327.
45 H. L. Jiang, T. Akita and Q. Xu, *Chem. Commun.*, 2011, **47**, 10999–11001.
46 T. Peng, H. Wang, H. Yi, Y. Jing, P. Sun and X. Wang, *Electrochim. Acta*, 2015, **176**, 77–85.
47 Y. Yamada, K. Yano, Q. Xu and S. Fukuzumi, *J. Phys. Chem. C*, 2010, **114**, 16456–16462.
48 D. Lide, *CRC Handbook of Chemistry and Physics*, CRC Press LLC, Boca Raton, FL, 84th edn, 2003–2004, pp. 5–14.
49 C. Kittel, *Introduction to Solid State Physics*, John Wiley & Sons, Inc, Hoboken, NJ, 8th edn, 2005.
50 K. Oura, M. Katayama, A. V. Zotov, V. G. Lifshits and A. A. Saranin, *Surface science: An introduction*, Springer, 2003.
51 L. Dai, Q. Qin, P. Wang, X. J. Zhao, C. Y. Hu, P. X. Liu, R. X. Qin, M. Chen, D. H. Ou, C. F. Xu, S. G. Mo, B. H. Wu, G. Fu, P. Zhang and N. F. Zheng, *Sci. Adv.*, 2017, **3**, e1701069.
52 Y. Chang, M. L. Lye and H. C. Zeng, *Langmuir*, 2005, **21**, 3746–3748.
53 Z. Xi, J. Li, D. Su, M. Muzzio, C. Yu, Q. Li and S. Sun, *J. Am. Chem. Soc.*, 2017, **139**, 15191–15196.
54 C. C. Hou, W. F. Fu and Y. Chen, *ChemSusChem*, 2016, **9**, 2069–2073.
55 Z. Xiao, Y. Wang, Y. C. Huang, Z. Wei, C. L. Dong, J. Ma, S. Shen, Y. Li and S. Wang, *Energy Environ. Sci.*, 2017, **10**, 2563–2569.

56 L. Zhang, P. F. Liu, Y. H. Li, C. W. Wang, M. Y. Zu, H. Q. Fu and X. H. Yang, *ACS Catal.*, 2018, **8**, 5200–5205.
57 L. Köhler and G. Kresse, *Phys. Rev. B: Condens. Matter Mater. Phys.*, 2004, **70**, 165405.
58 D. Özhava and S. Özkar, *Appl. Catal., B*, 2016, **181**, 716–726.
59 P. Li, Z. Xiao, Z. Liu, J. Huang, Q. Li and D. Sun, *Nanotechnology*, 2015, **26**, 025401.
60 R. Garcıía-Muelas, Q. Li and N. López, *ACS Catal.*, 2015, **5**, 1027–1036.
61 T. Choksi, P. Majumdar and J. P. Greeley, *Angew. Chem., Int. Ed.*, 2018, **57**, 15410–15414.